Particle Acceleration in Interacting Magnetic Flux Ropes

IOP Conf. Series: Journal of Physics: Conf. Series **1100** (2018) 012009 doi:10.1088/1742-6596/1100/1/012009

Particle Acceleration in Interacting Magnetic Flux Ropes

Senbei Du[1], Gary P. Zank[1,2], Fan Guo[3,4], Xiaocan Li[3], Adam Stanier[3]

[1] Department of Space Science, University of Alabama in Huntsville, Huntsville, AL 35899, USA

[2] Center for Space Plasma and Aeronomic Research (CSPAR), University of Alabama in Huntsville, Huntsville, AL 35805, USA

[3] Los Alamos National Laboratory, Los Alamos, NM 87545, USA

[4] New Mexico Consortium, Los Alamos, NM 87544, USA

E-mail: sd0050@uah.edu, garyp.zank@gmail.com, fanguo.ustc@gmail.com

Abstract. Magnetic flux ropes (or magnetic islands) are ubiquitous space plasma structures. Recent observations suggest that they are often associated with the acceleration of charged particles, but detailed acceleration mechanisms remain unclear. In this study, we present PIC simulations studying particle acceleration due to magnetic flux ropes. We consider a simple 2D configuration of two-magnetic-island coalescence. Some electrons and protons are found to be accelerated to more than 10 times their initial kinetic energies at the end of the simulation. We use a particle tracing technique on the high-energy particles to clarify the associated acceleration mechanisms. We find that reconnection electric field and Fermi-type acceleration due to magnetic island contraction can explain the particle energy gain, which is consistent with previous simulation studies. Our results also suggest that electrons are more responsive to the island contraction mechanism compared to ions. An effective island contraction rate is derived from the simulation data. Finally we briefly discuss a statistical description of particle acceleration associated with interacting magnetic flux ropes, and how it can be connected to simulations.

1. Introduction

Magnetic flux ropes are structures characterized by helical magnetic field lines. They are referred to as magnetic islands when viewed in 2D, where magnetic field lines form closed-loop-like structures. Magnetic flux ropes are frequently observed in space plasmas, such as in the Earth's magnetosphere [1, 2] and in the solar wind [3–5].

Magnetic reconnection, which is a sudden change in magnetic field configuration, plays a crucial role in the formation and evolution of magnetic flux ropes. Numerous simulations suggest that magnetic islands are formed in an elongated reconnecting current sheet. Multiple magnetic islands may be generated in a 2D turbulent reconnecting flow, and they undergo dynamic evolution such as coalescence and merging [e.g., 5–8]. Observational studies appear to support the view that small scale flux ropes in the solar wind are generated by the local magnetic reconnection and turbulent processes [3–5].

An interesting aspect of magnetic flux ropes is their potential to accelerate charged particles. Despite Gosling et al. [9] find that direct magnetic reconnection is not an efficient particle accelerator in the solar wind, recent observations suggest that magnetic flux ropes may be

responsible for particle acceleration in the heliosphere. Khabarova et al. [5] discuss the crossing of the heliospheric current sheet (HCS) by interplanetary shocks. They find that atypical energetic particle events downstream of the shocks can be associated with small-scale magnetic flux ropes. Khabarova & Zank [10] reexamined the "Gosling event" [9] and 126 related events over a larger time and more extended spatial range and energies. They found evidence of an energetic particle population, most likely accelerated by turbulence/magnetic island related structures generated by the initial reconnection events. In these regions, magnetic flux ropes undergo dynamic interactions through magnetic reconnection. Particles that are trapped in such regions can be accelerated more efficiently than in an isolated reconnection exhaust.

Numerical simulations have suggested several mechanisms for particle acceleration. The basic processes include first order Fermi acceleration due to magnetic island contraction, and direct acceleration by the reconnection electric field generated during the merging of two adjacent magnetic islands [11–15]. Zank et al. [16] develop a theoretical particle transport equation that describes the particle acceleration in a sea of interacting magnetic islands, incorporating the abovementioned basic acceleration mechanems. le Roux et al. [17] derive a more sophisticated transport equation from a quasi-linear approach, where the energization is associated with guiding center drift motions. The two equations discuss the same energization mechanisms but in terms of field line contraction and guiding center motions. However, both theories need to be tested against more careful simulations and observations. In return, detailed simulation studies will enable us to better understand the acceleration processes, and thus guide the development of more sophisticated transport models.

In this study, we perform fully kinetic particle-in-cell (PIC) simulations of the coalescence of two magnetic flux ropes. We use a particle tracing technique to study the acceleration of both electrons and ions. We report some findings regarding the acceleration mechanisms, recognizing the limitation of a 2D model, and discuss the connection between simulations and a statistical transport theory.

2. Simulation Model

The simulation uses the VPIC code [18], which solves Maxwell's equations for electromagnetic fields and the relativistic equations of motion for particles. The simulation setup is reported in an earlier work (Du et al., in preparation). The initial configuration contains two magnetic islands embedded in a reconnecting current sheet, illustrated in the top left panel of Figure 1. A similar setup has also been used in several previous simulation studies [e.g., 19–21]. The magnetic field is given by

$$B_x = \frac{B_0 \sinh(z/L)}{\cosh(z/L) + \varepsilon \cos(x/L)};\ B_z = \frac{B_0 \sin(x/L)}{\cosh(z/L) + \varepsilon \cos(x/L)};\ B_y = \frac{B_0\sqrt{1-\varepsilon^2}}{\cosh(z/L) + \varepsilon \cos(x/L)},$$

where L is the distance between the two islands, which also determines the system size, and ε is a measure of the island size. This setup ensures that the initial condition is force free, i.e., $\mathbf{J} \times \mathbf{B} = (\nabla \times \mathbf{B}) \times \mathbf{B} = 0$. The simulation box is set to $x \in [-2\pi L, 2\pi L]$, $z \in [-\pi L, \pi L]$. We set $L = 2d_i$ and $\varepsilon = 0.4$ in the simulation, where $d_i = c/\omega_{pi}$ is the ion inertial length. A periodic boundary condition is applied to the x direction, whereas conducting field/reflective particle boundaries are used in the z direction. We consider only an electron–proton plasma, and the mass ratio m_i/m_e is set to 25. The initial electron and proton temperatures are uniform throughout the simulation domain with $kT_e = kT_i = 3.75 \times 10^{-3} m_e c^2$. The magnetic field strength B_0 is determined by the ω_{pe}/Ω_{ce} value, where $\omega_{pe} = \sqrt{4\pi n_0 e^2/m_e}$ and $\Omega_{ce} = m_e c/eB_0$ are the electron plasma frequency and electron gyrofrequency, respectively. We set $\omega_{pe}/\Omega_{ce} = 2$ in our simulations. The particle number density profile is also uniform initially. The initial plasma beta is then given by $\beta_e = \beta_i = n_0 kT_e/(B_0^2/2) = 0.03$. About 400 macro-particles per cell are used for each species.

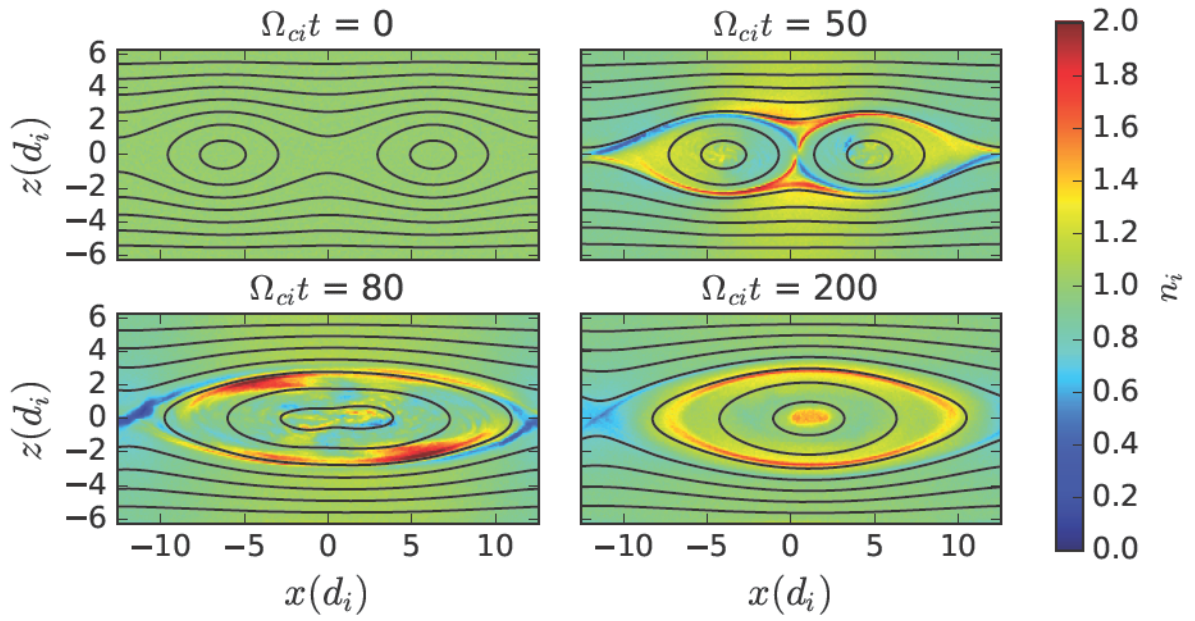

Figure 1. Snapshots at four normalized time, showing the ion number density, on which in-plane magnetic field lines are superimposed.

3. Results

3.1. Methodology

Figure 1 shows several snapshots of the ion number density on which in-plane magnetic field lines are superimposed. The general evolution and the energy conversion of the system is addressed in a previous study (Du et al., 2018, in preparation), so we do not discuss them here. In this paper, we focus on particle energization using a particle tracing technique. We present a detailed analysis of tracer particle trajectories and discuss the acceleration mechanisms for both electrons and ions.

A total of 4×10^8 macro-particles (including both electrons and ions) are used in the simulation, and we select 2×10^4 particles as tracers during the first run. To save storage space, the tracer trajectories are not well resolved in time. We then select the highest-energy tracers and run the simulation a second time to obtain better time-resolved particle trajectories. The energy selection criteria is $E_e \gtrsim 7.8 \times 10^{-2} m_e c^2$ for electrons, and $E_i \gtrsim 5.3 \times 10^{-2} m_e c^2$ for ions, where E_e and E_i are the kinetic energy of the tracer particles at the end of the simulation. We find a total of 131 electrons and 86 ions that satisfy the criteria, and obtain their trajectories.

As discussed in Zank et al. [16], the basic particle acceleration mechanisms associated with flux ropes include island contraction and reconnection electric field. A simple way to model the island contraction mechanism is by using adiabatic invariants. For a contracting magnetic island, assuming a compressible process, the conservation of first and second adiabatic invariants, as well as the magnetic flux yield the rate of change in particle momentum

$$\frac{\mathrm{d}p_\parallel}{\mathrm{d}t} = \eta_c p_\parallel; \quad \frac{\mathrm{d}p_\perp}{\mathrm{d}t} = \frac{1}{2}\eta_c p_\perp. \tag{1}$$

On the other hand, if we assume the coalescence of magnetic islands is an incompressible process, i.e., the total area of the islands remains the same after coalescence, then the rate of change of

particle momentum becomes

$$\frac{\mathrm{d}p_\parallel}{\mathrm{d}t} = \eta_m p_\parallel; \quad \frac{\mathrm{d}p_\perp}{\mathrm{d}t} = -\frac{1}{2}\eta_m p_\perp. \tag{2}$$

Here, η_c and η_m are the associated island contraction rates for the compressible and incompressible magnetic island contraction cases, respectively. We adopt this simple model to analyze the simulation data.

3.2. Electron Acceleration

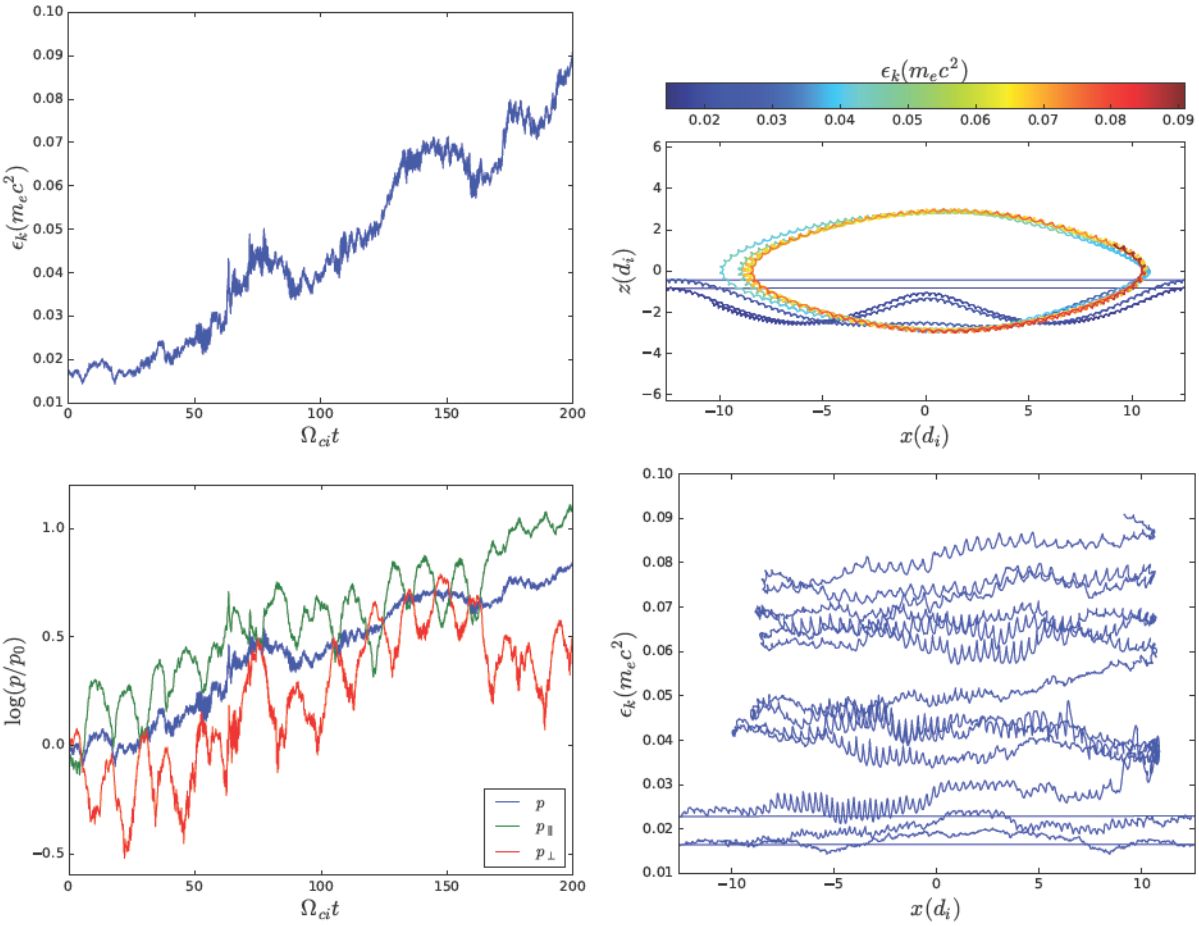

Figure 2. An example of an electron tracer. Top left: particle kinetic energy vs. time; bottom left: logarithm of normalized momentum (parallel, perpendicular and total) vs. time; top right: particle trajectory in the x-z plane; bottom right: particle kinetic energy vs. x-coordinate.

Some examples of electron trajectories are shown in Figures 2–5. To illustrate the acceleration mechanisms, we plot the kinetic energy vs. time (top left), momentum vs. time (bottom left), trajectory in the x-z plane (top right), and kinetic energy vs. x-coordinate (bottom right). Particle trajectories are color-coded by the corresponding kinetic energy. Since we apply a periodic boundary condition in x direction, a horizontal line appears in the trajectories and energy vs. time plots (right panels) when a particle crosses the x-boundaries. The momentum plots include both the parallel and perpendicular momenta, and also the total momentum. We plot them logarithmically as $\log(p/p_0)$, where p_0 is the momentum (parallel, perpendicular,

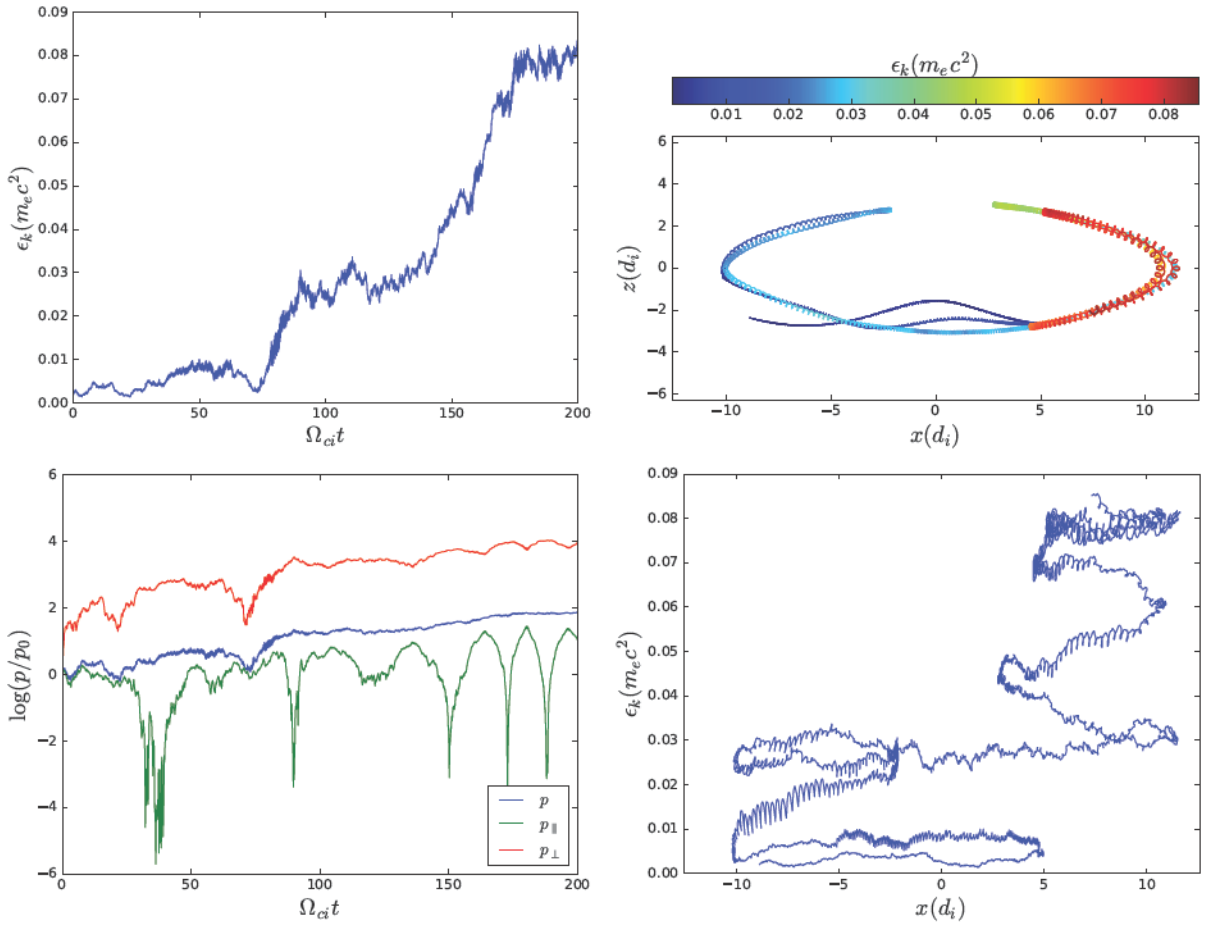

Figure 3. An example of an electron tracer. The format is the same as Figure 2

or total) at the initial time. As discussed below, this helps us understand the acceleration mechanisms. The momentum plots have been smoothed using a running average.

Figure 2 shows a tracer electron that undergoes acceleration due to magnetic island contraction. The particle energy increases as it orbits the flux ropes. As seen in the bottom left panel, both parallel and perpendicular momenta increase until nearly the end of the simulation when the perpendicular momentum drops. The linear increase in the particle momentum log(p) indicates that this is a first-order Fermi mechanism (as discussed later).

Figure 3 is another example of first-order Fermi acceleration, although the particle behaves differently than in the previous case. Here the particle is reflected several times inside the flux ropes, due to its small parallel momentum. The particle gains energy during the process because the length of the field lines is shortening.

Besides the island contraction (or Fermi acceleration) mechanism, we also see direct acceleration by the reconnection electric field. In Figure 4, the particle energy and momentum show a sudden increase at $\Omega_{ci}t \sim 75$. The bottom right panel shows that the sudden increase happens when the particle is near the boundary in the x direction. The trajectory also suggests that the particle is not trapped by the flux ropes before merging, but it is then trapped inside the single merged island at later time. Since the acceleration happens at the primary reconnection location, we attribute the main acceleration mechanism to the electric field generated by the primary reconnection event. Figure 5 is another example of a sudden energy increase at

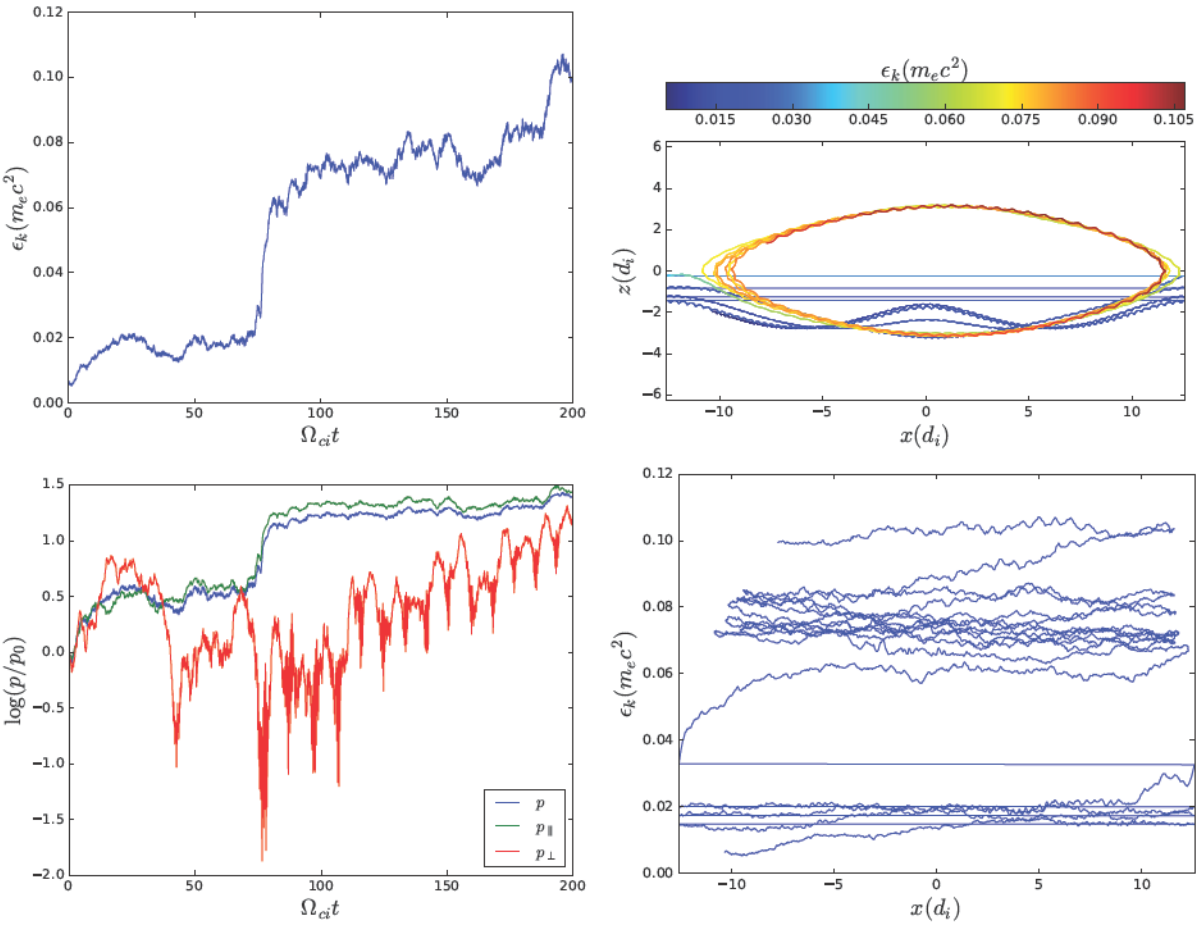

Figure 4. An example of an electron tracer. The format is the same as Figure 2

$\Omega_{ci}t \sim 75$. However, the acceleration site is near $x = 0$, where the island coalescence happens. Therefore, the reconnection electric field generated during coalescence is likely to be responsible for the particle energy gain. Since this electric field is in the opposite direction to the electric field generated by the primary reconnection event (near the x boundary of the simulation domain), it is called an anti-reconnection electric field in some literature [14, 16]. We also notice that in both examples that illustrate direct acceleration by reconnection electric fields, the particle energy continue to increase after the main merging phase. This suggests that the single merged magnetic island undergoes contraction, which leads to addition Fermi acceleration of particles, although the effect is not as large as the electric field energization for these two particular particles.

3.3. Ion Acceleration

Now we consider ion tracers. We find that the basic acceleration mechanisms are still the same—magnetic island contraction and reconnection electric field. Here we show examples of ion acceleration in Figures 6–8 in the same format as the previous plots.

In Figure 6, the ion energy increases suddenly at about $\Omega_{ci}t \sim 55$. From the trajectory, the main acceleration site is near the center of the simulation domain, where island coalescence occurs. This is consistent with direct acceleration by the anti-reconnetion electric field. The particle energy continues increasing after merging, due to island contraction.

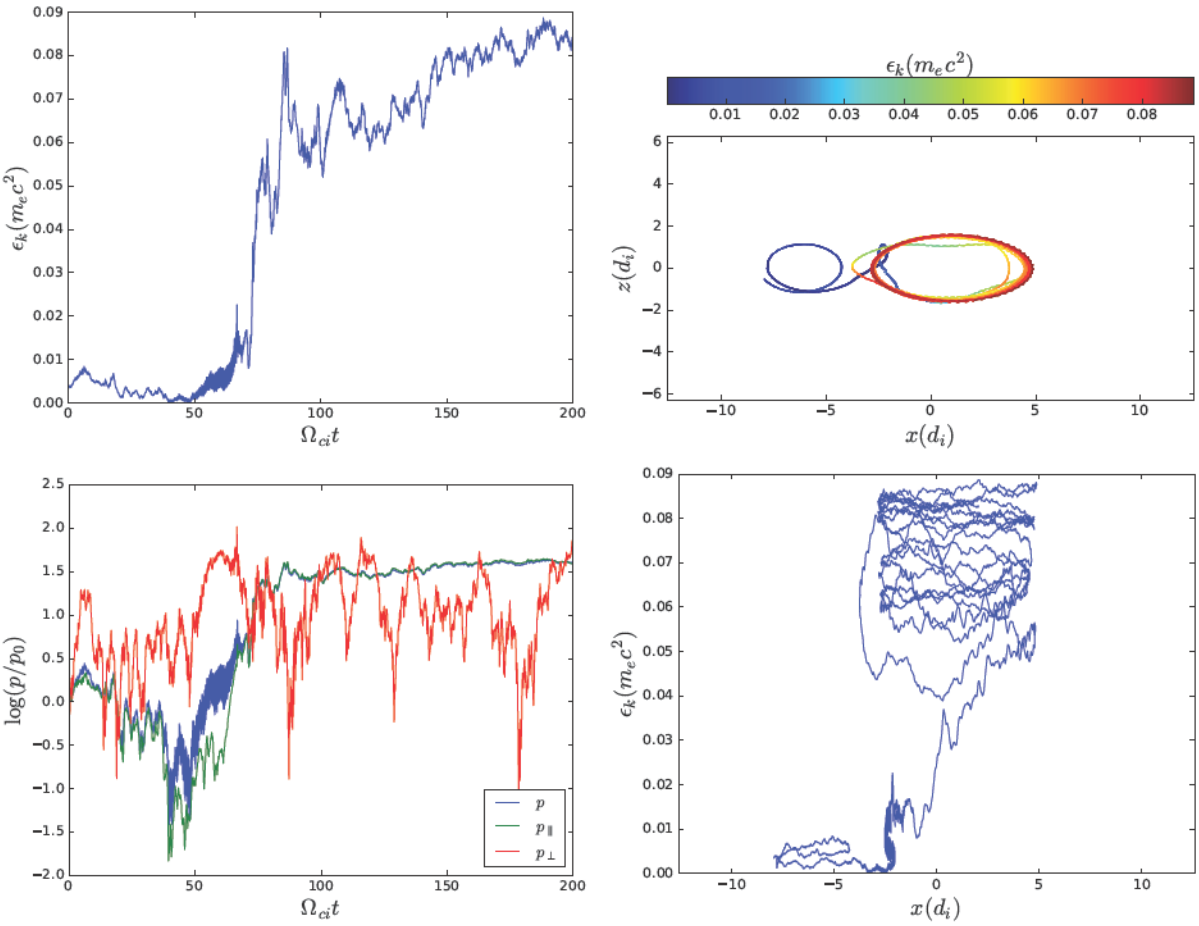

Figure 5. An example of an electron tracer. The format is the same as Figure 2

As a second example, in Figure 7, the ion gains energy at about $\Omega_{ci}t \sim 75$, near the location of primary reconnection. The particle is then trapped in the merged island, and undergo a reflection while gaining energy. The acceleration after island merging can still be interpreted as a first-order Fermi process.

Another interesting finding is that the kinetic energy does not necessarily increase after the main coalescence phase ends. Some of the ion tracers appear to undergo significant deceleration during later times of the simulation. An example is shown in Figure 8. In this case, the particle is accelerated to a high energy before $\Omega_{ci}t \sim 75$, which is likely due to the anti-reconnection electric field. It then experiences a gradual deceleration, and loses about half of its maximum kinetic energy by the end of the simulation. The deceleration seems to suggest a expanding magnetic island, which is inconsistent with the examples discussed before, so the mechanism is still not clear.

4. Discussion and Conclusions

4.1. Differences between Electron and Ion acceleration

We now discuss differences between the electron and ion acceleration. Since ions are much heavier than electrons, their gyroradii are much larger than those of electrons, especially after they are energized. As indicated by the tracer trajectories, the ion gyroradii approach scales comparable to the magnetic island size or the length scale on which the field varies. The large

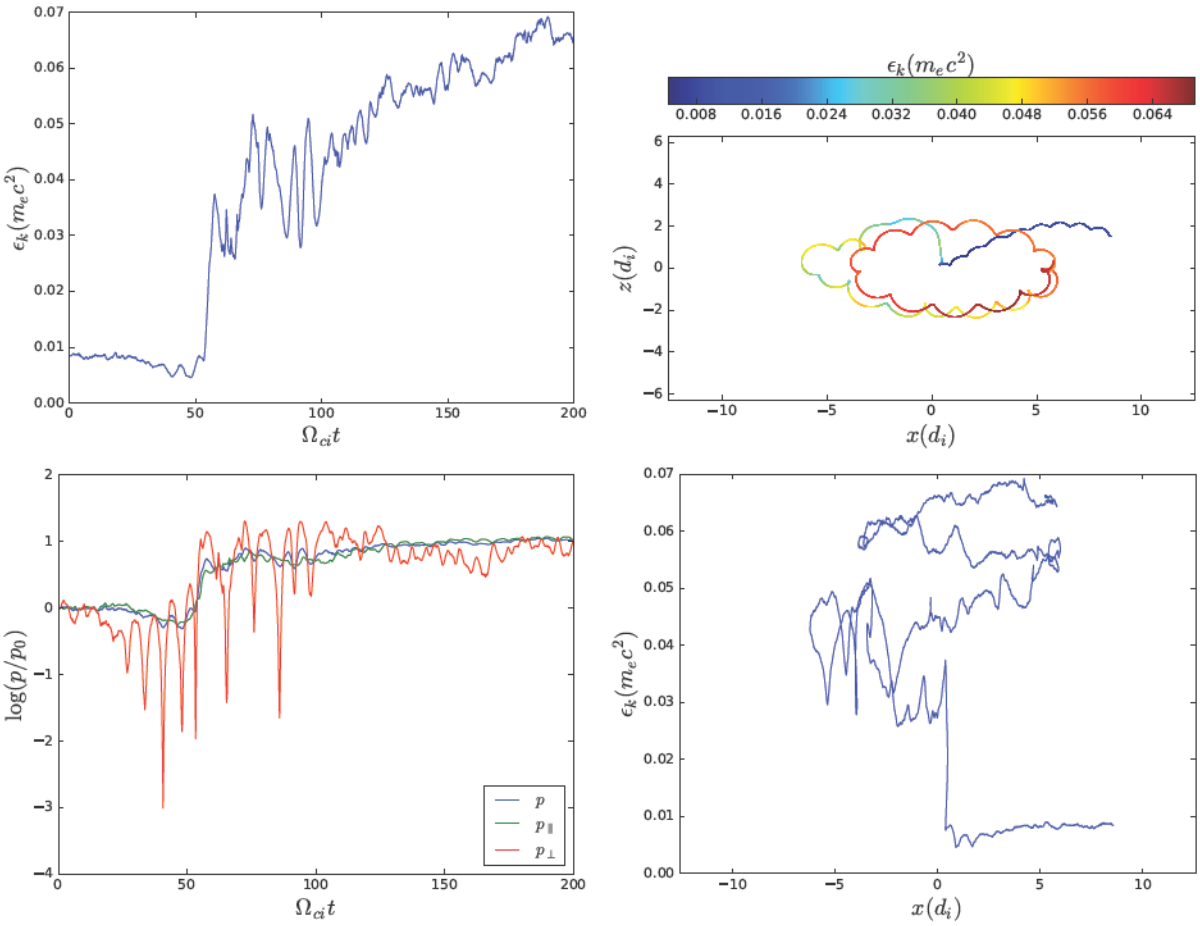

Figure 6. An example of an ion tracer. The format is the same as figure 2

gyroradii and gyroperiod may violate the conservation of adiabatic invariants, which may pose a problem on estimating the acceleration rate from the simple Zank et al. model [16]. We caution that the current simulation size is relatively small compared to the scale size of magnetic flux ropes observed in the solar wind. For example, recent observations [22] find that the scale size of observed small-scale magnetic flux ropes is $\sim 0.001 - 0.01$AU at a heliocentric distance of 1AU, which corresponds to $\sim 2\times10^3 - 2\times10^4 d_i$ on assuming a proton number density of $n_i = 10\text{cm}^{-3}$. The proton gyroradii could be much smaller compared to the flux rope sizes, and may behave like electrons. However, the plasma beta in the solar wind is usually larger than the value used in the simulation, which will result in a larger gyroradius.

A noticeable difference between ion and electron behavior is that ions are mostly accelerated during the main merging phase. This can be seen in the evolution of the total particle energy of the system (Figure 9). Electrons, while being accelerated at the merging time, continue to gain energy after the two islands merge. Since island contraction is the main acceleration mechanism after merging, we may infer that this mechanism seems to have a bigger impact on electrons than ions. Also we note that the simulation produces more high-energy electrons than ions, and the highest energy achieved by an electron tracer ($0.153 m_e c^2$) is slightly larger than that achieved by an ion tracer ($0.140 m_e c^2$). This difference may also be a consequence of the large ion gyroradii or the small simulation size. Interestingly, our previous study (Du et al., 2018, in preparation) shows that the macroscopic behavior is not much different in larger-size simulations

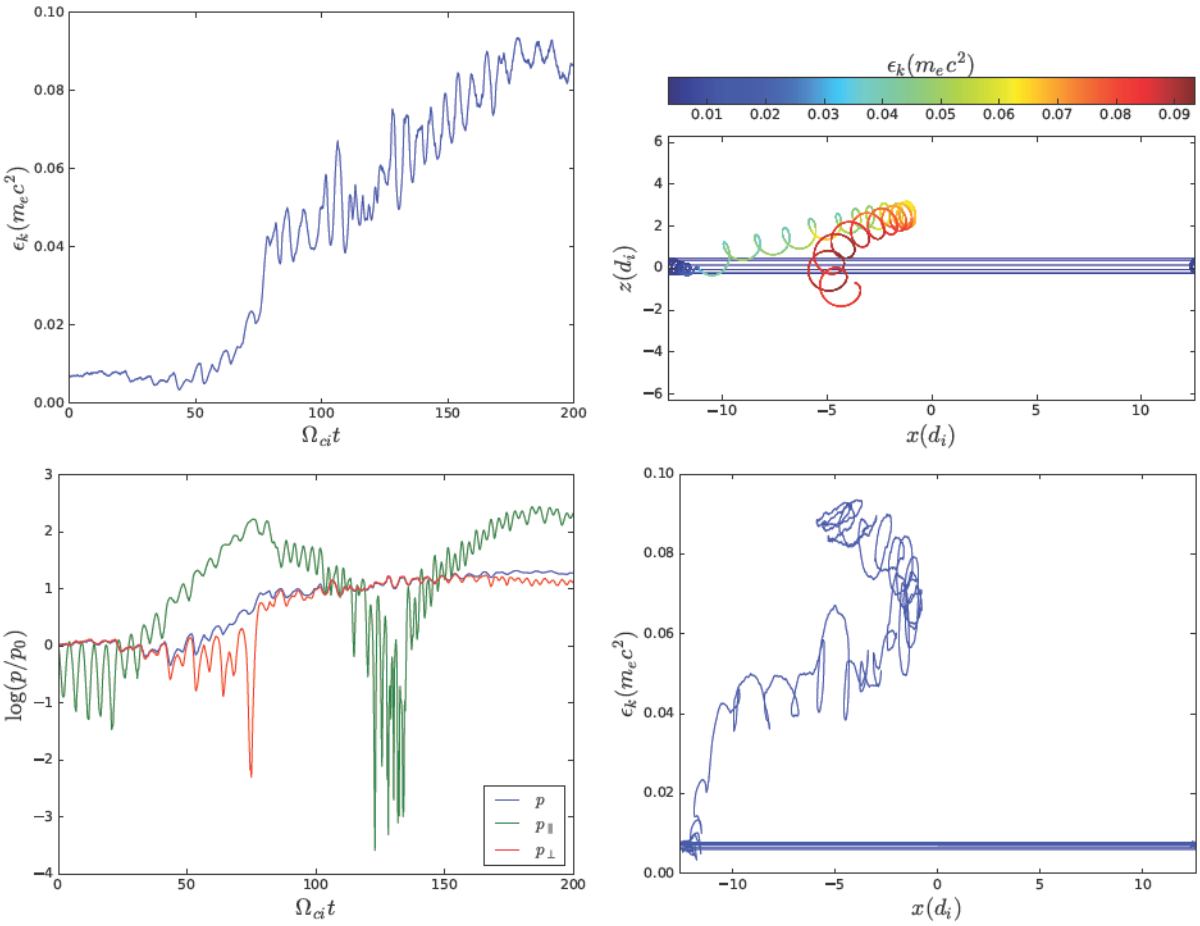

Figure 7. An example of an ion tracer. The format is the same as figure 2

(up to $\sim 100d_i$). A particle tracing study with larger simulations may be helpful.

Since magnetic island contraction is responsible for the particle acceleration during the later half of the simulation, we attempt to obtain an acceleration rate from the simulation data. We adopt the simple Zank et al. model [16], i.e., equations 1 and 2. Upon defining momentum logarithms $\xi_\parallel = \log(p_\parallel/p_{\parallel,0})$ and $\xi_\perp = \log(p_\perp/p_{\perp,0})$ where $p_{*,0}$ $(* = \parallel, \perp)$ are suitable constants, the equations can be rewritten in terms of new variables as

$$\frac{\mathrm{d}\xi_\parallel}{\mathrm{d}t} = \eta_c; \quad \frac{\mathrm{d}\xi_\perp}{\mathrm{d}t} = \frac{1}{2}\eta_c \tag{3}$$

for a compressible process, and

$$\frac{\mathrm{d}\xi_\parallel}{\mathrm{d}t} = \eta_m, \quad \frac{\mathrm{d}\xi_\perp}{\mathrm{d}t} = -\frac{1}{2}\eta_m \tag{4}$$

for an incompressible process. These expressions show that the slope of a $\log(p)$ vs. t curve gives an acceleration rate (or island contraction/merging rate). We observe from the $\log(p)$ vs. t plots that either the parallel or perpendicular momentum often includes large fluctuations. Therefore, we consider only the total momentum evolution. By transforming the variables $\xi_\parallel$ and $\xi_\perp$ to a total momentum logarithm $\xi = p/p_0$ and a pitch angle cosine $\mu = p_\parallel/p$, it is straightforward to

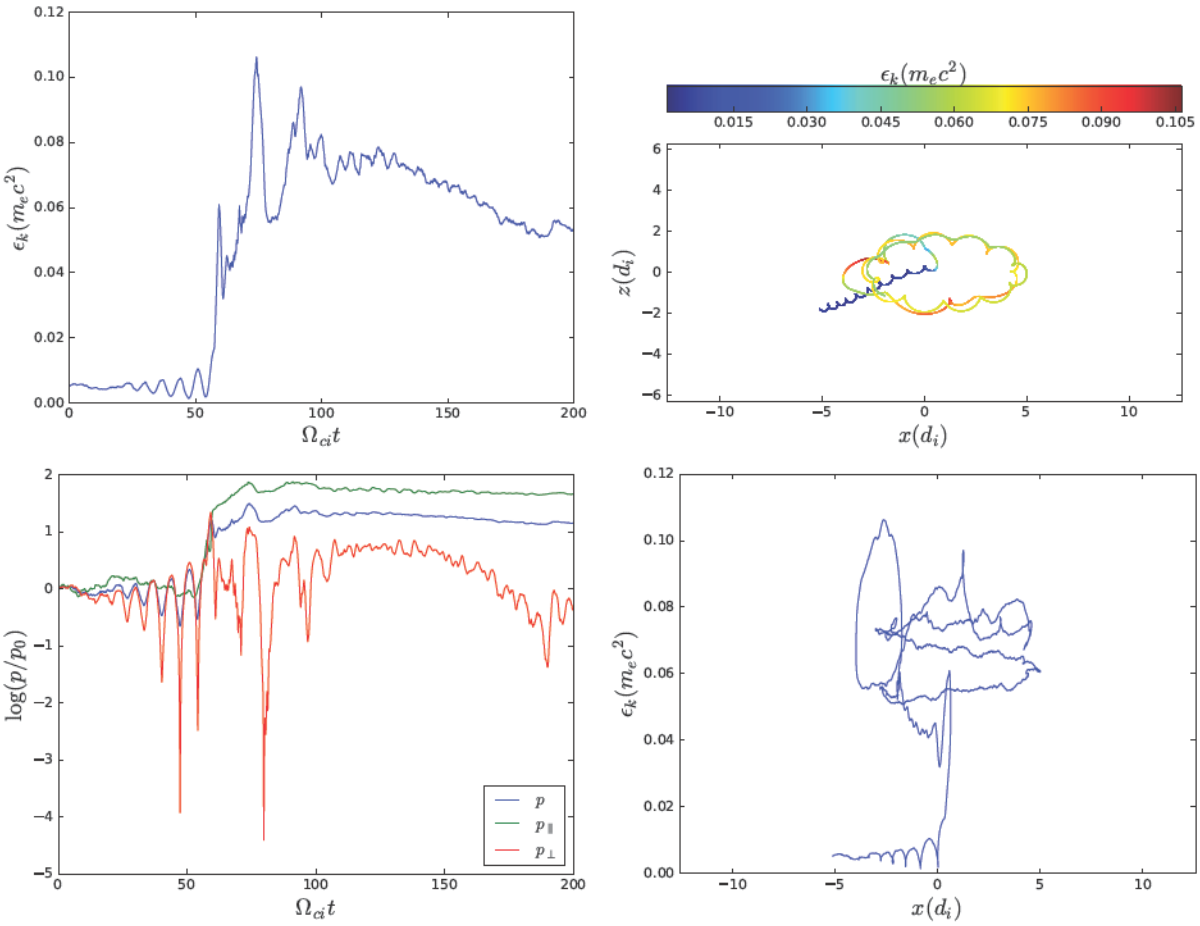

Figure 8. An example of an ion tracer. The format is the same as figure 2

convert equations 3 and 4 to

$$\frac{\mathrm{d}\xi}{\mathrm{d}t} = \frac{1}{2}\eta_c(1+\mu^2); \quad \frac{\mathrm{d}\mu}{\mathrm{d}t} = \frac{1}{2}\eta_c\mu(1-\mu^2); \tag{5}$$

$$\frac{\mathrm{d}\xi}{\mathrm{d}t} = \frac{1}{2}\eta_m(3\mu^2-1); \quad \frac{\mathrm{d}\mu}{\mathrm{d}t} = \frac{3}{2}\eta_m\mu(1-\mu^2), \tag{6}$$

for compressible and incompressible processes, respectively. Assuming the contraction/merging rates $\eta_{c/m}$ are independent of ξ and μ, we can obtain the rate of total momentum change after averaging the above equations over particle pitch angles. The resulting equations are formally written as

$$\frac{\mathrm{d}\xi}{\mathrm{d}t} = \tilde{\eta}_{c/m} \tag{7}$$

where $\tilde{\eta}_{c/m}$ is an effective contraction/merging rate that has absorbed the average of the pitch angle part of Equations (5) and (6). Note that in both compressible and incompressible cases, the changing rate of pitch angle cosine $d\mu/dt$ has the same sign as μ itself. This means that the pitch angle will increase in time for positive μ, and decrease for negative μ, aligning particle motions with the magnetic field, which may lead to an anisotropic particle distribution. However, suppose the particle distribution remains isotropic for some reasons (for example, due to particle scattering by background turbulence or self-generated waves), one concludes that $\tilde{\eta}_m = 0$ because

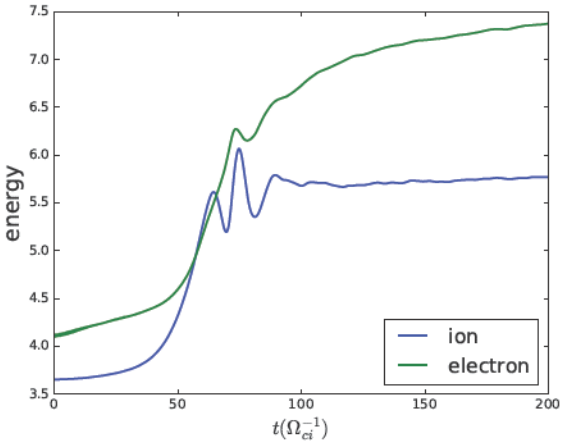

Figure 9. Total particle energy evolution of the system for ions and electrons. This plot includes all particles and not just the tracer particles.

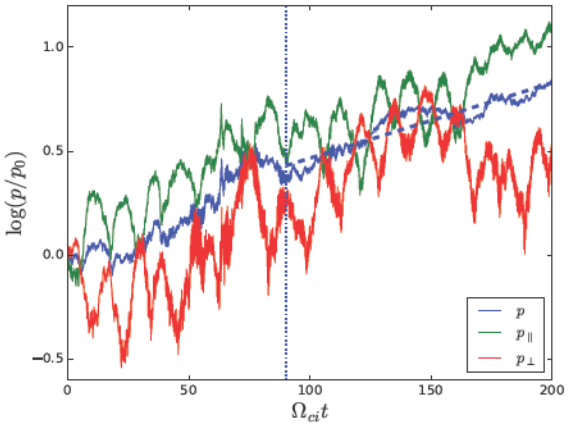

Figure 10. A linear fit to the $\log(p)$-t curve, corresponding to the same tracer electron as Figure 2. The dotted blue line indicates the starting time of the fit $\Omega_{ci}t = 90$, and the dashed blue line is the best fit to the solid blue curve (total momentum).

the integration of $3\mu^2 - 1$ is zero in Equation 6. More generally, we can expand the particle distribution in terms of Legendre polynomials [16]. Since the second-order Legendre polynomial is $P_2(x) = (3x^2 - 1)/2$, the only contributing term to the zeroth-order distribution function will be the second-order term. On the other hand, $\tilde{\eta}_c$ always has the same sign with η_c regardless of the particle distribution, as suggested by equation 5. Whether it is positive or negative depends on the dynamics of the flux rope: it may either be contracting or expanding. In this sense, one may call the compressible energization (η_c effect) first-order Fermi acceleration, and the incompressible energization (η_m effect) second-order Fermi acceleration or stochastic acceleration. In reality, one may expect both compressible and incompressible effects contribute to the acceleration of particles. We simply use Equation 7 in our analysis, and denote the acceleration rate as $\tilde{\eta}_c$, though it may be a combination of the η_c and η_m effects.

As discussed in the previous section, at early simulation times, particle acceleration is strongly affected by the reconnection electric field, so we apply a linear fit to $\log(p)$-t plots from the later part of the simulation, $\Omega_{ci}t = 90$ to $\Omega_{ci}t = 200$. Figure 10 illustrates our fitting procedure, where the same tracer electron as in Figure 2 is plotted. The fitting procedure is applied to all tracer electrons and ions, and a slope is obtained for each tracer. In Figure 11, we plot the pitch angle cosine at $\Omega_{ci}t = 90$, denoted as μ_1, against the acceleration rate $\tilde{\eta}_c$. Electron and ion tracers are plotted separately in the left and right panel. A mean value and a standard deviation are calculated and included in the figure. The fitting results show that electrons experience clear acceleration during the considered time interval, while ions are less strongly accelerated. This is consistent with Figure 9 and our previous discussion. Note that the fitting is only applied to the highest energy tracer particles, and the selection criteria is higher for electrons, so we caution about the potential bias in the analysis. One may also notice that electron pitch angles are strongly clustered near $\mu = -1$. This is mostly due to the initial setup of the simulation, because the initial force-free condition is achieved by introducing a particle drift motion along the magnetic field.

Tracer trajectories show that all the high energy electrons are trapped within the flux rope, although some of them are not trapped initially (such as the example shown in Figure 2). The trapping and escape of particles is very important for the acceleration process. For a particle to

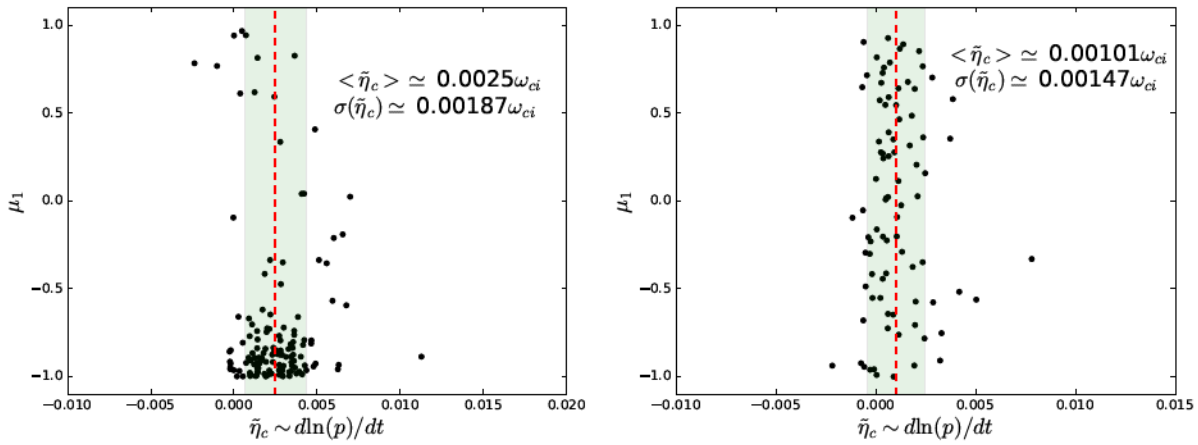

Figure 11. Scatter plots of acceleration rates for electrons (left) and ions (right). μ_1 is the pitch angle cosine at the start time of the fitting ($\Omega_{ci}t = 90$), and $\tilde{\eta}_c$ is the slope of $\log(p/p_0)$-t curves. The red dashed vertical line shows the mean value of $\tilde{\eta}_c$, and the shaded area shows the range $< \tilde{\eta}_c > \pm\sigma(\tilde{\eta}_c)$.

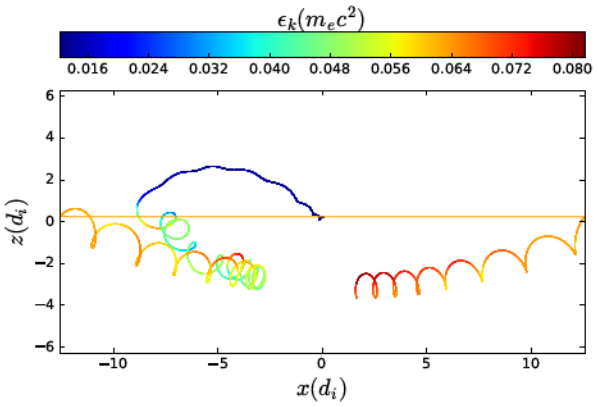

Figure 12. The trajectory of an ion tracer that escaped a flux rope.

gain energy in a contracting magnetic island via field line shortening, it needs to be trapped in the island. Escape is important for the formation of a power law energy spectrum by stochastic acceleration. In our simulation, high-energy electrons do not escape once they are trapped. This is likely due to the 2D nature of the simulation, as indicated by previous simulations [23]. Despite the large ion gyroradii, most of the ion tracers are also trapped within the flux rope. We find one case where an initially trapped ion seems to be scattered out of the flux rope after merging (shown in Figure 12). However, the escape mechanism is still not clear. We will return to this point later when we discuss the associated transport formalisms.

4.2. A Statistical Description of Particle Acceleration

In this section, we discuss briefly a statistical description of particle acceleration associated with multiple magnetic flux ropes. Similar to our previous analysis, we consider the island contraction mechanism only, and use the simple relation (Equation (7)) to estimate the particle momentum rate of change. The problem of stochastic acceleration can be treated as a random walk in momentum space. The classical approach to study the problem is to use the Fokker–Planck

(FP) equation

$$\frac{\partial f(\xi,t)}{\partial t} = -a\frac{\partial f(\xi,t)}{\partial \xi} + D\frac{\partial^2 f(\xi,t)}{\partial \xi^2}. \tag{8}$$

By using the FP equation, we essentially assume that the random walk is a Markov process, and the steps have a finite mean and variance, so that the coefficients are given by $a =< \Delta\xi > /\Delta t$ and $D =< \Delta\xi^2 > /2\Delta t$, where $< \Delta\xi >$ and $< \Delta\xi^2 >$ are the mean and variance of the momentum increment, and Δt is the time increment. Using equation (7), we can estimate the coefficients as

$$a \simeq < \eta_c >; \quad D \simeq < \eta_c^2 > \tau \tag{9}$$

where $< \eta_c >$ and $< \eta_c^2 >$ is the mean and variance of the acceleration rate, and τ is a characteristic time scale.

A transport equation of the FP type is applied to the flux rope acceleration problem by Bian & Kontar [24]. A more general approach is the so called continuous time random walk (CTRW). Depending on the form of the distribution of the acceleration rate and waiting time, the CTRW approach yields different forms of the transport equation (see, for example, Metzler & Klafter [25] for a comprehensive review). In the simplest case, the classical FP equation can be recovered, while in some other circumstances, a fractional differential equation (FDE) is more suitable. The idea of CTRW is that the step size (or jump length) and the waiting time between two steps (jumps) are drawn from a joint probability density function (pdf). If we further assume that the jump length is independent of the waiting time, each following a pdf $\lambda(\xi)$ and $\psi(t)$, then the governing equation for the particle distribution function can be written as a modified Chapman–Kolmogorov equation,

$$f(\xi,t) = \int_{-\infty}^{\infty} d\xi' \int_0^t dt' f(\xi',t')\lambda(\xi-\xi')\psi(t-t') + f_0(\xi)\int_t^{\infty} dt'\psi(t'). \tag{10}$$

It is often more convenient to work with the Fourier and Laplace transformed equation,

$$\hat{f}(k,u) = \frac{1-\hat{\psi}(u)}{u}\frac{\hat{f}_0(k)}{1-\hat{\lambda}(k)\hat{\psi}(u)}, \tag{11}$$

where we introduce a Fourier transform $\xi \to k$, and a Laplace transform $t \to u$ [25]. Considering only the island contraction mechanism, from Equation (7), the momentum change during a given time interval Δt is approximately

$$\Delta\xi = \eta_c \Delta t, \tag{12}$$

where we have dropped the tilde over η_c for notational simplicity. Suppose the effective contraction rate η_c has a pdf $g(\eta_c)$, then the jump length pdf is connected to η_c according to

$$\lambda(\Delta\xi)d\Delta\xi = g(\eta_c)d\eta_c. \tag{13}$$

On combining the two equations above,

$$\lambda(\xi) = \frac{1}{\Delta t}g\left(\frac{\xi}{\Delta t}\right). \tag{14}$$

Equation (14) provides a direct relation between the jump length pdf required for a CTRW process and the island contraction rate.

From our discussion, one sees that a theoretical description of stochastic acceleration is based on the distribution of acceleration rates $g(\eta_c)$. Our particle tracing technique provides a tool for obtaining such information, as the effective contraction rate $\tilde{\eta}_c$ associated with a flux rope

can be obtained from tracer particles. Currently we don't have any statistical information of magnetic islands in our current simulation, because there is only one coalescence event. However, we expect that in a large-scale multiple island simulation, a similar technique may be useful. Besides the acceleration rate, the waiting time pdf $\psi(t)$ is also important for determining the shape of the transport formalism in CTRW. Another important parameter is the acceleration time Δt in Equation (14), which may be interpreted as the characteristic trapping time of a particle by a contracting flux rope. Information about the waiting time and trapping time will be difficult to obtain, since in the current simulation most energetic particles are very efficiently trapped by flux ropes and rarely escape. This is where 3D vs. 2D simulations may be important. A future study of the trapping and escape mechanism will be important.

In summary, we carried out a 2D PIC simulation of the coalescence of two magnetic flux ropes. The analysis of tracer particle trajectories shows that the basic acceleration mechanisms are the reconnection electric field and magnetic island contraction. The primary particle acceleration mechanism is magnetic island contraction at late times. However, the reconnection or anti-reconnection electric field is important at early times when the islands coalescence happens, and it may contribute to most of the ion energy increase and a large portion of the electron energy increase. The island contraction mechanism seems to be more important for electrons than for ions, but this conclusion may depend on parameters such as the island size distribution and in terms of simulations, the box size. Effective island contraction rates are obtained from tracer particle data. Although we are not able to derive a full particle transport equation from the current simulation, we expect that the particle tracing technique will be useful for future theoretical developments of the transport formalism.

Acknowledgments

G.P.Z. and S.D. acknowledge the partial support of an NSF DOE grant PHY - 1707247 and a NASA grant SV4 - 84017. This material is based also in part upon work supported by the NSF EPSCoR RII-Track-1 Cooperative Agreement OIA-1655280. F. G. and X. L. acknowledge the support by NASA under grant NNH16AC60I, DOE OFES, and the support by the DOE through the LDRD program at LANL. F.G.s contributions are also partly supported by the U.S. Department of Energy, Office of Fusion Energy Science, under Award Number DE-SC0018240 and by the National Science Foundation under grant No. 1735414. G.P.Z. acknowledges the generosity of the International Space Science Institute (ISSI) in supporting him through the 2017 Johannes Geiss Fellowship. This work is also partly supported by the International Space Science Institute (ISSI) in the framework of International Team 504 entitled Current Sheets, Turbulence, Structures and Particle Acceleration in the Heliosphere. We thank Jakobus le Roux for the useful discussion. The simulations were performed at Los Alamos National Laboratory, and this research used resources of the National Energy Research Scientific Computing Center, a DOE Office of Science User Facility supported by the Office of Science of the U.S. Department of Energy under Contract No. DE-AC02-05CH11231.

References

[1] Wang R, Lu Q, Nakamura R, Huang C, Du A, Guo F, Teh W, Wu M, Lu S and Wang S 2016 *Nature Physics* **12** 263–267

[2] Huang S Y, Retino A, Phan T D, Daughton W, Vaivads A, Karimabadi H, Zhou M, Sahraoui F, Li G L, Yuan Z G, Deng X H, Fu H S, Fu S, Pang Y and Wang D D 2016 *J. Geophys. Res.* **121** 205–213

[3] Cartwright M L and Moldwin M B 2010 *J. Geophys. Res.* **115** A08102

[4] Zheng J and Hu Q 2018 *Astrophys. J.* **852** L23 (*Preprint* 1801.01771)

[5] Khabarova O, Zank G P, Li G, le Roux J A, Webb G M, Dosch A and Malandraki O E 2015 *Astrophys. J.* **808** 181 (*Preprint* 1504.06616)

[6] Servidio S, Matthaeus W H, Shay M A, Cassak P A and Dmitruk P 2009 *Phys. Rev. Lett.* **102** 115003

[7] Greco A, Matthaeus W H, Servidio S, Chuychai P and Dmitruk P 2009 *Astrophys. J.* **691** L111–L114

[8] Zank G P, Adhikari L, Hunana P, Shiota D, Bruno R and Telloni D 2017 *Astrophys. J.* **835** 147

[9] Gosling J T, Skoug R M, Haggerty D K and McComas D J 2005 *Geophys. Res. Lett.* **32** L14113

[10] Khabarova O V and Zank G P 2017 *Astrophys. J.* **843** 4

[11] Drake J F, Swisdak M, Che H and Shay M A 2006 *Nature* **443** 553–556

[12] Drake J F, Swisdak M, Schoeffler K M, Rogers B N and Kobayashi S 2006 *Geophys. Res. Lett* **33** L13105

[13] Drake J F, Swisdak M and Fermo R 2013 *Astrophys. J.* **763** L5 (*Preprint* 1210.4830)

[14] Oka M, Phan T D, Krucker S, Fujimoto M and Shinohara I 2010 *Astrophys. J.* **714** 915–926 (*Preprint* 1004.1154)

[15] Le A, Karimabadi H, Egedal J, Roytershteyn V and Daughton W 2012 *Phys. Plasmas* **19** 072120

[16] Zank G P, le Roux J A, Webb G M, Dosch A and Khabarova O 2014 *Astrophys. J.* **797** 28

[17] le Roux J A, Zank G P, Webb G M and Khabarova O 2015 *Astrophys. J.* **801** 112

[18] Bowers K J, Albright B J, Yin L, Bergen B and Kwan T J T 2008 *Phys Plasmas* **15** 055703

[19] Stanier A, Simakov A N, Chacón L and Daughton W 2015 *Phys. Plasmas* **22** 101203

[20] Stanier A, Daughton W, Chacón L, Karimabadi H, Ng J, Huang Y M, Hakim A and Bhattacharjee A 2015 *Phys. Rev. Lett.* **115** 175004

[21] Stanier A, Daughton W, Simakov A N, Chacón L, Le A, Karimabadi H, Ng J and Bhattacharjee A 2017 *Phys. Plasmas* **24** 022124 (*Preprint* 1611.05933)

[22] Zheng J, Hu Q, Chen Y and le Roux J 2017 *Journal of Physics: Conference Series* **900** 012024

[23] Dahlin J T, Drake J F and Swisdak M 2017 *Phys. Plasmas* **24** 092110 (*Preprint* 1706.00481)

[24] Bian N H and Kontar E P 2013 *Phys. Rev. Lett.* **110** 151101 (*Preprint* 1302.6090)

[25] Metzler R and Klafter J 2000 *Phys. Reports* **339** 1 – 77 ISSN 0370-1573